

Linear-Mode HgCdTe Avalanche Photodiodes for Photon-Counting Applications

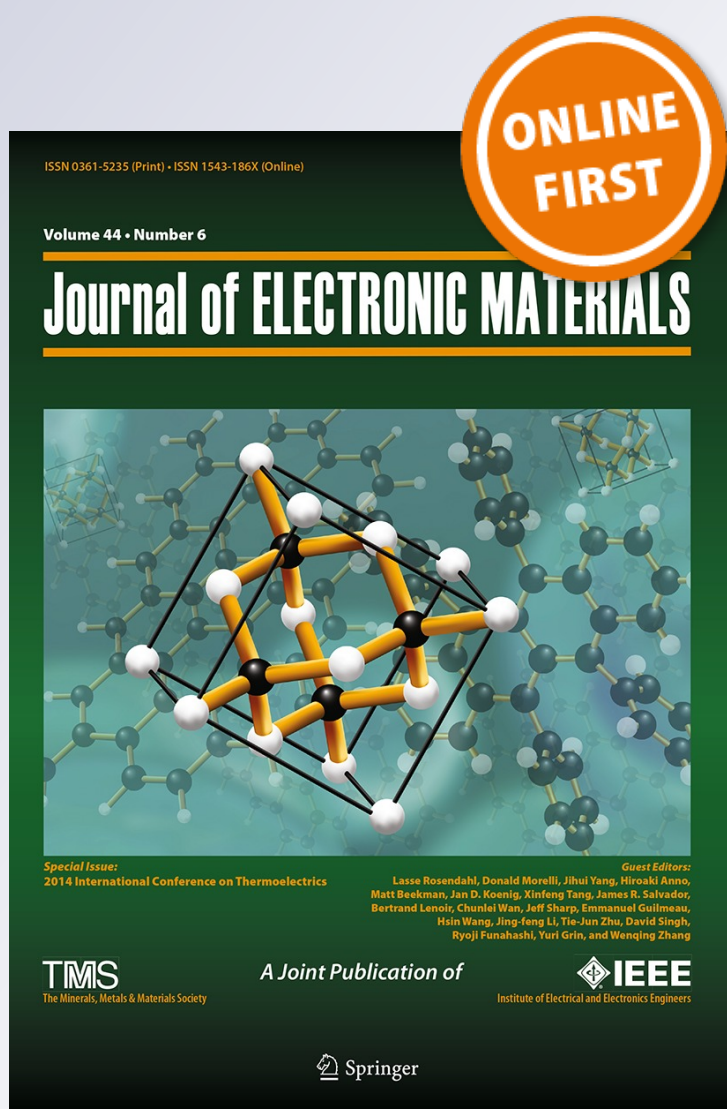
William Sullivan, Jeffrey Beck, Richard Scritchfield, Mark Skokan, Pradip Mitra, Xiaoli Sun, James Abshire, Darren Carpenter, et al.

Journal of Electronic Materials

ISSN 0361-5235

Journal of Elec Materi

DOI 10.1007/s11664-015-3824-3



Your article is protected by copyright and all rights are held exclusively by The Minerals, Metals & Materials Society. This e-offprint is for personal use only and shall not be self-archived in electronic repositories. If you wish to self-archive your article, please use the accepted manuscript version for posting on your own website. You may further deposit the accepted manuscript version in any repository, provided it is only made publicly available 12 months after official publication or later and provided acknowledgement is given to the original source of publication and a link is inserted to the published article on Springer's website. The link must be accompanied by the following text: "The final publication is available at link.springer.com".

Linear-Mode HgCdTe Avalanche Photodiodes for Photon-Counting Applications

WILLIAM SULLIVAN III,^{1,4} JEFFREY BECK,¹
RICHARD SCRITCHFIELD,¹ MARK SKOKAN,¹ PRADIP MITRA,¹
XIAOLI SUN,² JAMES ABSHIRE,² DARREN CARPENTER,³
and BARRY LANE³

1.—DRS Technologies, C4ISR Group, 13544 N. Central Expressway, Dallas, TX 75243, USA.
2.—NASA Goddard Space Flight Center, Greenbelt, MD 20771, USA. 3.—A/DIC Inc., 740 Florida
Central Parkway, Longwood, FL 32750, USA. 4.—e-mail: billy.sullivan@drs.com

An overview of recent improvements in our understanding of, and the maturity of, linear-mode photon counting with the HgCdTe electron-initiated avalanche photodiode is presented. In 2010 DRS fabricated an experimental 2×8 array with $(64 \mu\text{m})^2$ pixels which enabled, for the first time, linear-mode photon counting by use of the MWIR cutoff HgCdTe electron-initiated avalanche photodiode. The device had a high single-photon signal-to-noise ratio of 13.7, an excess noise factor of 1.3–1.4, a 7 ns minimum time between events, and a broad spectral response extending from 0.4 μm to 4.2 μm . DRS recently fabricated a new set of devices with improved yield and performance compared with the first device: the false event rate was reduced by a factor of almost 10 to 150 kHz, the photon detection efficiency was increased from 50% to >60%, and the APD gain was increased by a factor of 4 to over 1900.

Key words: Avalanche photodiode, HgCdTe, single-photon counting, mid-wave infrared, photon detection efficiency, false-event rate

INTRODUCTION

Mid-wave infrared (MWIR) HgCdTe electron-initiated avalanche photodiodes (e-APDs) with single-photon sensitivity have many applications including photon counting, ladar and lidar, quantum cryptography, and free space optical communication links. Photodiode receivers with single-photon sensitivity have significant device and system level benefits, for example enabling reduction of the optical source's size, weight, and power requirements as fewer received photons are required for detection. APDs are operated in two different modes: Geiger mode and linear mode. Geiger-mode APDs are biased above their breakdown voltage and the breakdown process is initiated on absorption of a single photon, resulting in an

avalanche gain in the millions. As such, they require a quenching circuit to stop the breakdown process and reset the circuit. This quenching action requires a finite amount of time (typically tens of nanoseconds to 1 μs), and leaves the detector blind to another incoming photon for that amount of time. Compared with Geiger-mode APDs, linear-mode APDs are biased below the breakdown voltage. Because breakdown does not occur, there is no deadtime and quenching circuits are not required. Gains are typically on the order of 10–10,000. The output of the linear-mode APD is a linear sum of all the photon responses without such nonlinear effects as deadtime. Photons that are coincident on the APD generate an output voltage that is proportional to the number of incident photons, and photons that are closely spaced in time produce a train of closely spaced output pulses. The timing resolution between individual photons, also called the minimum time between events (MTBE), is limited by the combined bandwidth of the APD and the pre-amplifier, and is currently pre-amplifier bandwidth-limited at

(Received January 21, 2015; accepted April 30, 2015)

Table I. Comparison of key performance characteristics of the 2010 array and the 2013 arrays

Performance characteristic	2010 LMPC array	Two 2013 arrays	
		A8327-8-2	A8327-14-1
1. False event rate at 50% PDE	> 1 MHz	151 kHz	158 kHz
2. Maximum APD gain	470	1910	1100
3. Maximum photon detection efficiency	50%	72%	66%
4. Electrical bandwidth	71 MHz	71 MHz	71 MHz

8–10 ns.^{1,2} DRS previously reported cylindrical geometry linear-mode photon-counting (LMPC) e-APDs in a 2×8 format array, with robust photon counting performance by use of the MWIR HgCdTe e-APD.^{1,2} Under a recent NASA Earth Science Technology Office (ESTO) Advanced Component Technology (ACT) program three device improvements were implemented to increase performance, and the maturity of photon counting technology, with DRS's MWIR e-APDs. In the 2010 array, the false event rate* (FER) with the thresholds set for 50% photon detection efficiency** (PDE) was over 1 MHz, while an adjacent test pixel's gain-normalized dark current was only 30 k electrons/s. It was concluded that this large discrepancy between expected and measured FER was caused by the array APDs absorbing photons emitted from the readout integrated circuit (ROIC) which artificially increased the FER, because the test pixels were mounted on a passive fanout that did not have active photon-generating devices under them. This was improved in 2013 by depositing a metal blocking layer on top of the ROIC to shield the detectors from the glow photons. The next improvement was to increase the device's maximum PDE by reducing the APD junction diameter (i.e., reducing the multiplication region diameter, shown in Fig. 2), and by using improved measurement techniques. Reducing the junction diameter reduced the APD's excess noise factor and increased the maximum APD gain from 470 at 13 V bias in the 2010 device to over 1900 in a 2013 device. The third improvement was to use an alternative *p*-type contact process which substantially improved the array yield compared with 2010. The key performance characteristics of the arrays are compared in Table I.

*The term "false event rate" is used as a cumulative term that combines all threshold-exceeding events caused by ROIC noise and detector "dark" current. The detector-induced events are those arising as a result of intrinsic detector dark current, current resulting from photons emitted by the ROIC, stray photons in the Dewar flask, and thermal background flux through the cold filter. The false event rate is measured without any intentional photon flux applied to detector.

**The term "photon detection efficiency" is the single photon detection efficiency of the entire detector including the APD and the ROIC, and is explained in the section "[Conversion Efficiency](#)".

AVALANCHE PHOTODIODE DESIGN

The 2013 arrays were fabricated in a similar fashion to the 2010 arrays.¹ Briefly, the APDs were fabricated in a 2×8 format array with a $64 \mu\text{m}$ pixel pitch from $\text{Hg}_{1-x}\text{Cd}_x\text{Te}$ grown by use of liquid phase epitaxy (LPE) with $x = 0.33$ for a cutoff of $4.3 \mu\text{m}$ at 77 K. Each pixel was composed of four parallel diodes in a 2×2 configuration. The arrays used DRS's high-density vertically integrated photodiode (HDVIPTM) architecture¹: a front face-illuminated *p*-around-*n* cylindrical homo-junction diode structure that features low capacitance for high bandwidth, low defect density, and interdiffused CdTe surface passivation on both array surfaces for low dark current. The arrays were fabricated on the same ROICs as were used on the 2010 LMPC arrays,¹ however, between the ROIC unit cells and the individual pixels, a photon blocking "mirror" metal layer was added to some of the FPAs as a process split to enable comparison of FERs between FPAs with and without the shield metal. Briefly, the custom Si ROIC features an analog output and a digital comparator output with individually settable thresholds for each pixel, although the digital outputs were not used in the testing reported here. Each pixel has a separate direct analog output pin and a direct digital output pin resulting in 32 ROIC outputs. The outputs are not multiplexed. The unit cell features an adjustable gain resistive transimpedance amplifier (RTIA) with a designed bandwidth of 175 MHz and a designed single-photon signal-to-noise ratio (SNR) of 23.2 at an APD gain of 1000. A simplified schematic diagram of a single ROIC channel is shown in Fig. 1; this highlights the analog signal path. During the NASA ACT program, long after the ROICs had been fabricated, a parasitic analysis performed on the ROIC by use of Silvaco Hipex revealed that unaccounted for stray capacitances in the unit cell's design limited the bandwidth and the full 175 MHz was not achieved. Simulations and measurements showed that the bandwidth was only approximately 71 MHz and the single-photon SNR was only 13.9, in good agreement with measured values given in the section "[MTBE and Pulse Width](#)" and discussed in more detail there. The Silvaco Hipex analysis also suggested techniques to reduce the parasitic effects in future ROICs to ensure the full designed bandwidth was obtained.

EXPERIMENTAL

The arrays were operated in a custom pour-fill LN₂ laboratory Dewar flask at 82 K that featured extensive shielding from stray light. This was implemented in an effort to reduce the FER and ensure the high FER measured in 2010 was not because of stray thermal background flux. Two cold filters, each with a pass band of 1.2–1.8 μm and >OD4 blocking from 2 μm to 5 μm (measured cold), were stacked to provide >OD8 out-of-band blocking with a combined 75% in-band transmission at 1550 nm. When an *f*/1.5 cold aperture was used the calculated combined in-band and out-of-band background count rate was 12.2 kHz, which corresponds to a background photon flux of 5×10^8 ph/(s cm²) assuming a net photon conversion efficiency of 60%. When performing optical tests with the laser, the system was calibrated to the detector surface (i.e. the cold filters' and window's transmissions were corrected for). Two different fiber-coupled lasers were used for characterization, a 1-ns pulsed laser and a cw laser. Both were 1550 nm, and they were not used simultaneously. The lasers were focused by use of a 0.42 numerical aperture (NA) objective lens mounted on a stepper-motor-controlled XYZ stage with sub-micron movement capability. This system was used to move the focused laser to the area of interest in the pixel, typically in the center *p*-type

HgCdTe region between the four junctions, as shown in Fig. 2. The spot size on the detector was focused to a full width at half maximum (FWHM) spot size of approximately 7 μm, by use of the 0.42 NA objective, and was determined by de-convolving the raw image with a user-generated point spread function and visually determining the best fit. The data shown in Figs. 7, 8, and 9 are raw measured PDE; they are not de-convolved images (Table II).

RESULTS

Five arrays were evaluated from the current 2013 batch, A8327, each with different processing splits. The splits enable characterization of the effects of a specific processing step while keeping all of the other processing steps the same. Four of the five arrays were Hg vacancy (*V*_{Hg}) doped with an *N*_A of $\sim 1 \times 10^{16}$ cm⁻³ and one was Cu + *V*_{Hg}-doped with an *N*_A of $\sim 2 \times 10^{16}$ cm⁻³. Four arrays had a single layer ZnS anti-reflection (AR) coating of 92% efficiency whereas one array had a double layer ZnS + SiO₂ AR coating of >98% efficiency. Finally, three arrays had a ROIC glow “mirror” blocking metal layer deposited directly under the HgCdTe pixels whereas two did not. All of the arrays received the same processing steps except for these splits. Table III summarizes the performance of five of the arrays, and Fig. 3 shows the 16-pixel-mean PDE as a function of FER for each array under a cw flux of 5×10^6 photons/s. The PDE was measured by recording 4 ms of each pixel's raw analog output sampled at 5×10^9 samples per second with the cw laser on and again with the laser off. Thresholding of the individual photon peaks was performed in software post-processing to calculate the event rate as a function of threshold for each waveform independently. The PDE was then calculated by subtracting the laser-off event rate (equivalent to the FER versus threshold) from the laser-on event rate at each threshold and then dividing by the cw laser flux. For example, if the detector had 100% PDE and a 100 kHz FER, then in 4 ms, 400 individual pulses

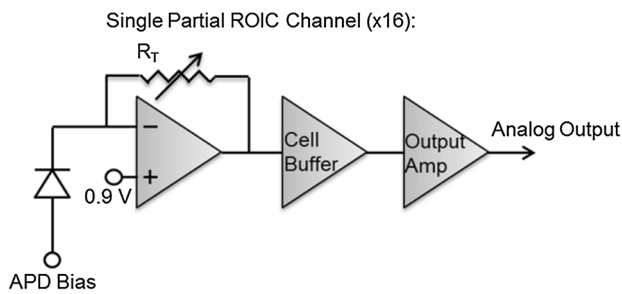


Fig. 1. Simplified single-channel ROIC architecture.

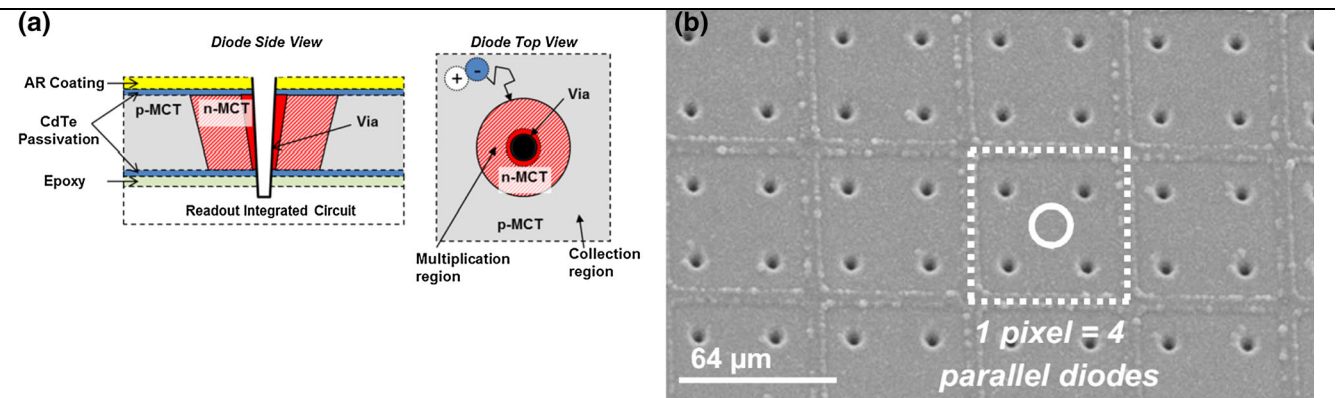


Fig. 2. (a) DRS's HDVIPTM diode geometry. (b) Scanning electron microscope array image of a similar HDVIPTM array with a single pixel's outline shown. One pixel is composed of 4 parallel diodes. The solid circle shows the typical focused laser illumination location.

Table II. Array processing splits

Array	<i>p</i> -type doping	ROIC glow mirror blocking metal layer	AR coating
A8327-2-2	V_{Hg}	Yes	ZnS
A8327-8-2	$Cu + V_{Hg}$	Yes	ZnS
A8327-14-1	V_{Hg}	Yes	ZnS
A8327-14-2	V_{Hg}	No	ZnS
A8327-20-2	V_{Hg}	No	ZnS + SiO ₂

Table III. 2010 and 2013 array performance summary

	Two 2013 arrays		
	2010 LMPC array	A8327-8-2	A8327-14-1
<i>p</i> -Type doping	V_{Hg}	$Cu + V_{Hg}$	V_{Hg}
Maximum PDE (focused spot)	50% (at 14 V APD bias)	72% (at 12.9 V)	66% (at 12.9 V)
APD gain	470 (at 13 V)	1910 (at 12.9 V)	1100 (at 12.9 V)
FER at 50% PDE	> 1 MHz	151 kHz	158 kHz
Mean single photon SNR	13.7	21.9	12.3
Excess noise factor	1.3–1.4	1.25	1.20
Measured RMS jitter	632 ps	2370 ps	1570 ps
Minimum time between events	8 ns	Not measured	9 ns

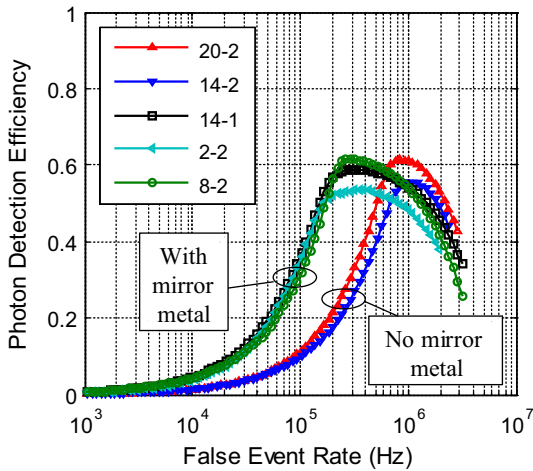


Fig. 3. Sixteen-pixel mean PDE as a function of FER for five different 2×8 arrays at an APD bias of 12.9 V and under a cw flux of 5×10^6 photons/s. A $5\times$ decrease in FER was observed for the three arrays with the mirror blocking metal compared with the two arrays without it.

would be expected in the laser-off waveform and 20,400 pulses would be expected in the laser-on waveform, where each pulse is caused either by a photon from the laser, stray flux, or a dark-current-generated electron. As the excess noise factor of the APD is > 1 , the amplitude of each pulse is gamma distributed, which introduces spread in the ROIC output voltage pulse amplitudes. At low thresholds more of the photon pulses cross the threshold and the PDE is higher, but the FER is also higher for the same reason. At higher thresholds, the FER is lower

because fewer of the pulses cross the threshold value, but the PDE is also reduced for the same reason.

A $5\times$ decrease in FER was observed for the three arrays with the mirror blocking metal compared with the two arrays without it, confirming that ROIC glow was indeed contributing to the FER. A8327-8-2 had a slightly higher maximum PDE, because of its expected longer electron diffusion length and higher gain compared with the other two V_{Hg} -only-doped samples with the mirror photon blocking metal layer. A8327-20-2 had a higher PDE than A8327-14-2, because of the more efficient AR coating. Overall, the higher PDEs shown in Fig. 3 are close to theoretical predictions and simulations.

False Event Rate

It has been shown that Si CMOS transistors in saturation emit photons because of hot carrier effects and the rate of emission is up to 10^4 higher at 80 K than at 300 K.³ In the vertically integrated structure that DRS uses, and without any metal blocking layers, these ROIC emitted photons are in the “direct line of sight” of the APD array and have energies within the detectors’ spectral response. Also, uncovered high-power buffers that were present around the perimeter of the ROIC (to drive the signals off-chip) were also very likely to be emitting photons. To validate that ROIC glow was indeed the major source of the FER increase, two sister arrays were fabricated in the 2013 batch from the same HgCdTe bar (wafer section): one without a metal mirror blocking layer (A8327-14-2) to simulate the 2010 array and one with a 96.9% coverage single

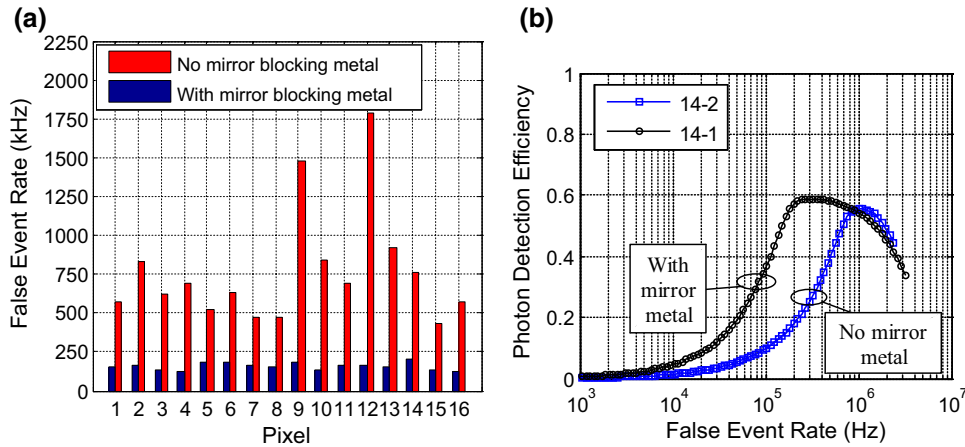


Fig. 4. (a) FER as a function of the number of pixels at the optimum threshold of 4.8 mV. (b) 16-pixel mean PDE as a function of FER, showing $\geq 50\%$ PDE for all pixels of both arrays at an FER of < 200 kHz.

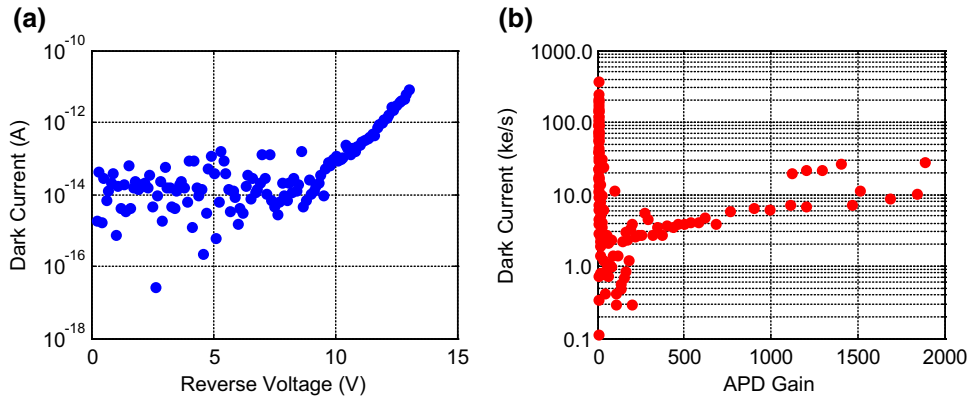


Fig. 5. (a) Measured dark current as a function of applied reverse voltage of a test pixel. (b) Gain normalized dark current of the same test pixel showing a maximum effective dark current of less than 30 k e/s at gains up to 1900.²

metal blocking layer (A8327-14-1) deposited on top of the ROIC before the HgCdTe was mounted. The properties of the HgCdTe across the bar were typically very uniform enabling comparison of the effect of the metal layer only and not the HgCdTe dark count rate. In Fig. 4, sixteen-pixel mean PDE as a function of FER is compared for A8327-14-1 and A8327-14-2. Each pixel's FER is ≤ 200 kHz for A8327-14-1, with an average FER of 158 kHz at the optimum threshold of 4.8 mV, yielding $PDE \geq 50\%$ for all pixels, as shown in Fig. 4. The 16-pixel average FER of A8327-14-2 was $4.8\times$ higher at 767 kHz. Optimization of the ROIC biases reduced A8327-14-1's FER by another factor of two, yielding almost an order of magnitude decrease in FER compared with the 2010 results. This provided further proof that ROIC glow was responsible for increasing the FER.

Although the FER was reduced, it still was not reduced to measured test diode gain normalized dark current levels of 30 k e/s or less, as shown in Fig. 5. This is probably because the metal layer was only a semi-continuous single layer and the perimeter buffers were not also covered by the mirror blocking metal. To reduce the FER to the measured diode dark current of

< 30 k e/s shown in Fig. 5, the ROIC must include several metal layers for 100% coverage directly under the detectors and blocking of the perimeter buffers.

Effect of Gain on PDE

The different PDE resulting from different *p*-type doping is shown in Fig. 6. A8327-8-2 has a 5% higher PDE, probably because of its higher gain. Because the excess noise factor for these diodes is ~ 1.2 to 1.3, a small portion of the initial photoelectrons do not receive full gain. In these instances the ROIC's output voltage pulse amplitude is reduced, and in some cases it is reduced so much that the pulses are below the ROIC's output noise floor. Higher gain results in ROIC output pulses with higher amplitudes so that the lower gained photoelectron pulses are not lost in the noise.

APD Junction Diameter and Multiplication Region Width

The APD's junction diameter is a critical factor determining the performance of the detector. For a given APD pitch (in the 2×2 APD pixel

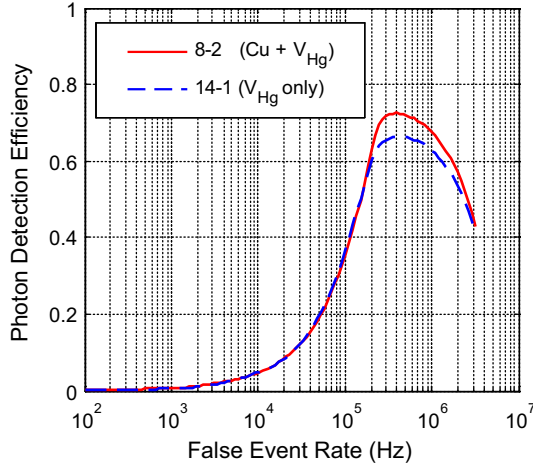


Fig. 6. PDE as a function of FER for different p -type doping.

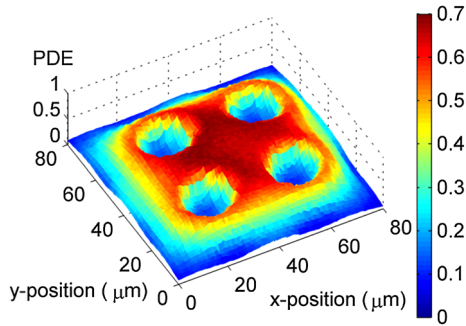


Fig. 7. PDE as a function of position inside a pixel of A8327-8-2. The central p -type area has the highest PDE. The PDE decreases inside the junctions because the gain falls off rapidly, and finally the lowest PDE is inside the metal vias.

configuration) the junction diameter determines the diffusion jitter and the electron collection efficiency (eCE), where the eCE is defined as the percentage of photoelectrons collected by the junctions. The APD gain is determined by the multiplication region width^{4,5} which, for the HDVIPTM structure, is determined by the junction and via diameters of the APD (cf. Fig. 2). The excess noise factor also depends on the multiplication region width.⁴

The PDE depends directly on the net photon-to-collected electron conversion efficiency. The photon conversion efficiency (PCE) is the product of the quantum efficiency (QE), the fill factor, and the eCE. The spatial dependence of the electron collection efficiency is revealed by performing response spot scans over the area of the pixel. High resolution, 1- μm -step, surface spot scans were performed on an operating pixel to measure PDE as a function of location in the pixel and also to determine the junction diameter. The 1550 nm cw laser was focused using a 0.42 NA long working distance objective lens to a spot size of approximately 7 μm FWHM diameter and scanned across the pixel. Figure 7 shows the PDE as a function of position

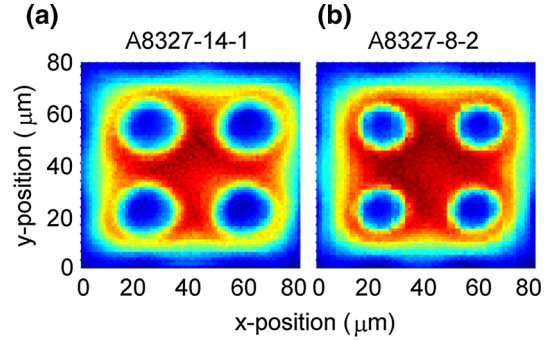


Fig. 8. Surface spot scan of PDE as a function of location for a single pixel in (a) A8327-14-1 and (b) A8327-8-2.

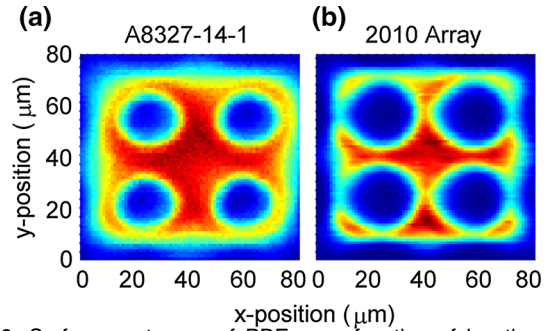


Fig. 9. Surface spot scan of PDE as a function of location for a single pixel in (a) A8327-14-1 and (b) 2010 array. This array had larger junctions because of a deliberate change in the junction-formation process.

spot scan for A8327-8-2. In Fig. 8, PDE as a function of position spot scan is compared for A8327-14-1 and A8327-8-2, and in Fig. 9 the V_{Hg} -doped sample is compared with the 2010 array, which was also V_{Hg} -doped. The junction diameter results are summarized in Table IV.

The $\text{Cu} + V_{\text{Hg}}$ -doped sample, A8327-8-2, has smaller junction diameters of approximately 22 μm whereas the V_{Hg} -doped only sample, A8327-14-1, has larger junction diameters of approximately 25 μm . This is expected, because $\text{Cu} + V_{\text{Hg}}$ -doped samples have smaller junctions than V_{Hg} -doped-only samples when etched under the same conditions, and etching was the same for all the arrays. Comparison of the spot scan data with those for the 2010 array revealed its junctions are even larger, at approximately 31 μm . Assuming an $n+$ diameter of 12 μm , A8327-8-2's junction width is approximately 5 μm , A8327-14-1's is 6.5 μm , and the 2010 array's is 9.5 μm . Larger-diameter junctions result in lower gain at the same APD bias voltage and, for the same diode pitch, lower jitter, and this is observed for the 2010 array. Larger junctions should also have a higher eCE (effectively maximum PDE) assuming the same diode pitch and electron diffusion length; however, the 2010 array did not have a higher PDE than the current arrays with smaller junctions. This is probably because of

Table IV. Summary of junction diameter, APD gain, rms jitter, maximum PDE, and excess noise factor for the three arrays

Array	Junction diameter (μm)	APD gain	Measured RMS jitter (ps)	Maximum PDE	Excess noise factor
2010 array	31	470 (@ 13 V)	632	0.5 (at 14 V APD bias)	1.30–1.40
A8327-14-1	25	1100 (@ 12.9 V)	1570	0.66 (at 12.9 V APD bias)	1.20
A8327-8-2	22	1910 (@ 12.9 V)	2370	0.72 (at 12.9 V APD bias)	1.25

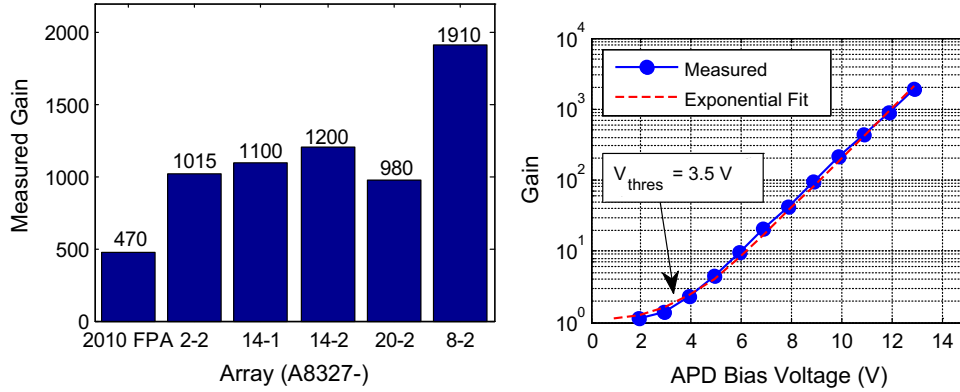


Fig. 10. Left: measured gain as a function of array at bias of 12.9 V. Right: measured and fit gain as a function of voltage for pixel 1,1 of A8327-8-2.

its lower gain and the more refined PDE as a function of FER algorithm that is currently being used. It may also be partially because of the slightly lower excess noise factors in the current arrays.

Gain

Increased APD gains of up 1910 were measured on the operating arrays by use of 1550 nm light focused in the middle of the four junctions, as shown in Fig. 10. The smaller measured junction width for A8327-8-2 agrees with the higher gain measured at the same bias voltage of 12.9 V. Gain across the four V_{Hg} -doped only arrays was uniform with a mean gain of $1073 \pm 12\%$.

Jitter

Jitter was measured by use of the pulsed laser focused in the middle of the four junctions. The leading edge of an external InGaAs photodiode was used as the time reference, and the time delay from when the leading edge of the analog output crossed a user-set threshold of 6 mV was measured by use of a LeCroy oscilloscope. 5000 pulses were accumulated for each jitter measurement. A8327-14-1's rms jitter was 1570 ps and A8327-8-2's was 2370 ps. On the 2010 array, the rms jitter was measured the same way and was 632 ps. The increase in jitter in the current devices is because of the smaller junction diameters, because the electron has a longer distance to diffuse, leading to a longer time delay and rms jitter. The rms jitter can be reduced by

placing the diodes on a closer pitch, and this will be implemented in future designs. A 3D Monte Carlo random-walk electron diffusion model yields good agreement with measured data; the results are summarized in Table V and Fig. 11.

Conversion Efficiency

As stated above, the net photon conversion efficiency of the pixel is the product of quantum efficiency (QE) in the pixel active area (which depends on wavelength, AR coating, and the HgCdTe thickness), the eCE, and the fill factor. In our case where we are using a focused spot in the p -region, the fill factor is 100%. For an HgCdTe detector 6 μm thick at 1550 nm the device's QE is 90–99%, depending on the AR coating. Modeling suggests the eCE is of the order of 80–90% yielding a maximum PDE of 70–90%, depending on diode geometry; this is in agreement with experimental results.

Excess Noise Factor

The excess noise factor of the avalanche photodiodes was determined by use of three methods:

- fitting the event rate as a function of threshold voltage data measured with cw flux as discussed in the section “PDE versus FER Model”;
- fitting photon pulse amplitude distribution data; and

Table V. Summary of the modeled and measured jitter and eCE

	A8327-8-2 ($V_{Hg} +$ Cu-doped)	A8327-14-1 (V_{Hg}-doped)	2010 array (V_{Hg}-doped)
Electron mobility (model input)	29,000 ($\text{cm}^2/(\text{Vs})$)	26,000 ($\text{cm}^2/(\text{Vs})$)	26,000 ($\text{cm}^2/(\text{Vs})$)
Diffusion length (equivalent electron lifetime) (model input)	20 μm (20 ns)	13 μm (9.4 ns)	13 μm (9.4 ns)
Junction diameter (model input)	21 μm	25 μm	31 μm
Simulated rms jitter	2.38 ns	1.50 ns	0.764 ns
Measured rms jitter	2.37 ns	1.57 ns	0.632 ns
Simulated eCE	83%	79%	91%
Calculated eCE (Measured $\text{PDE}_{\text{max}} * 1.08$ for AR coating efficiency)	77%	71%	54%

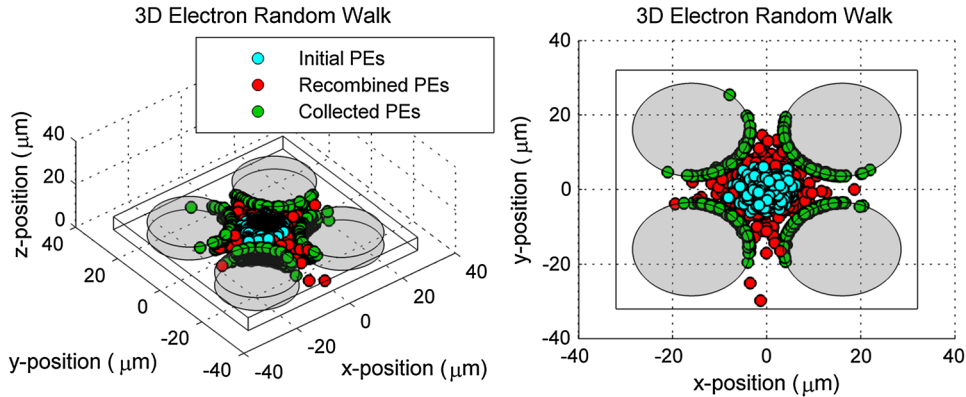


Fig. 11. 3D Monte Carlo random-walk simulation results. The simulation models diffusion of electrons in the p -type region and records how many photo-electrons (PEs) are collected, and how many recombine before diffusing into one of the junctions; it also measures the time-of-arrival statistics to determine the jitter.

- using the equation below with 1 ns pulses of increasing photon numbers where F is the excess noise factor, n is the number of photons per pulse, μ is the mean of the output pulse amplitudes, and σ is the standard deviation of the output pulse amplitudes.

$$F = \left(\frac{\sqrt{n}}{\frac{\mu}{\sigma}} \right)^2$$

Each method verified the single photon excess noise factor was 1.2–1.3. The pulsed PDE was measured for A8327-14-1 with an average of 1 photon/pulse, and good agreement was found in fitting of the data by use of an excess noise factor of 1.25, as shown in Fig. 12. The model calculates the overall probability density function by Poisson-weighting and convolving the individual photon probability density gamma functions along with the ROIC's output noise probability density function.

Signal-to-Noise Ratio

The measured SNRs are shown in Table VI. The mean single-photon pulse amplitudes and rms noise voltages reported both include the external electronics' gain of +5 V/V. The rms noise was uniform

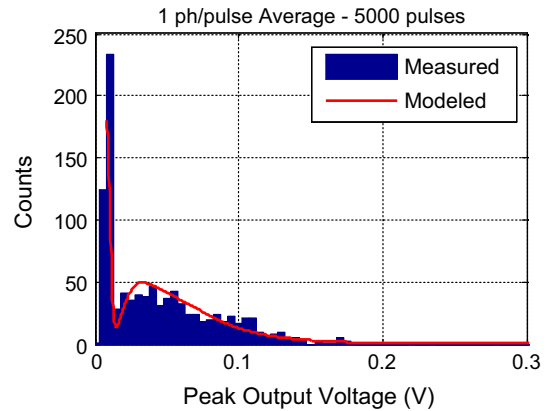


Fig. 12. Histogram of 5000 pulse amplitudes with a 1 photon/pulse input signal. The modeled curve is a noise factor of 1.25.

across all 16 pixels at 3 mV on both of the current arrays, and is higher than for the 2010 array because of reduction of the ROIC biases to reduce the rate of glow-emitted photons. This increased the rms noise, which only affects very low amplitude photon pulses, but, more importantly, reduced the rate of glow emitted photons, which reduced the overall FER.

Table VI. Summary of the mean single-photon SNR

Array	Bias (V)	APD Gain	Mean single photon voltage (mV)	RMS noise (mV)	Mean single photon SNR
2010 array	13	470	23.8	2.0	11.9
2010 array	14	Not measured	27.4	2.0	13.7
A8327-14-1	12.9	1100	37	3.0	12.3
A8327-8-2	12.9	1910	68	3.1	21.9

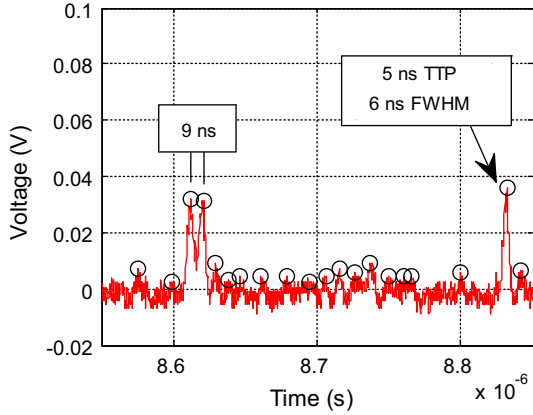


Fig. 13. Single analog output from A8327-14-1, measured with the LeCroy oscilloscope. Peaks were detected in software post-processing and are indicated by open circles. The APD bias was 12.9 V, and the ROIC RTIA gain was 125 k Ω . Pulses closer together than 10 ns are easily discernable.

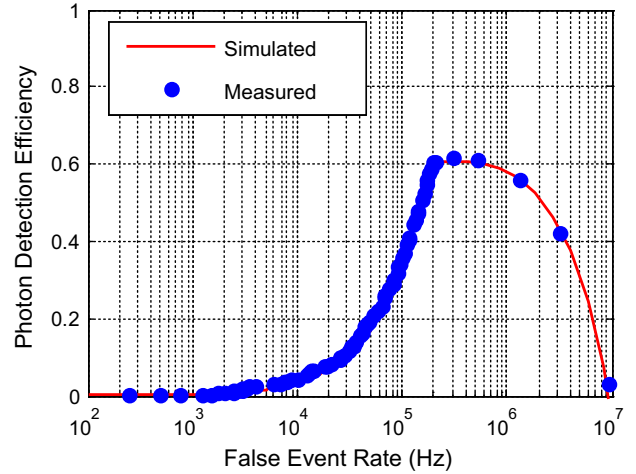


Fig. 14. Modeled and measured PDE as a function of FER for A8327-14-1 pixel 1,1.

MTBE and Pulse Width

At an ROIC RTIA gain of 125 k Ω , the minimum time between pulses was shown to be 9 ns, cf. Fig. 13. Typical output pulses had a time to peak (TTP) of 5 ns with a 10–90% rise time of approximately 3 ns. This is similar to previously reported results for the 2010 array. In many applications the pulse amplitude or area is used to derive the number of received photons and overall pulse shape. The MTBE is simply a measure of how closely in time two individual photons can be distinguished. The Silvaco Hipex parasitic extraction revealed that a significant amount of parasitic capacitance was present in the fabricated ROIC that was not accounted for in the design, limiting the electrical bandwidth and hence the TTP. Future designs of the ROIC will take the parasitic extraction analysis into account, enabling the full designed bandwidth to be achieved.

Operability

One pixel out of all the pixels on five of the arrays that were tested had a dark current greater than 1 nA resulting in operability of 98.75% for all of the arrays.

PDE VERSUS FER MODEL

A model was generated which explains the PDE as a function of FER, including the downwards trend after the peak PDE is reached. Good agreement with measured data was obtained, as shown in Fig. 14. The model generates an output voltage distribution for when the laser is on and for when the laser is off and then processes them exactly as the raw data are processed. Each voltage distribution comprised a gamma distribution for the excess noise factor of the APD added to a Gaussian distribution for the ROIC noise. The model provides a method to fit the excess noise factor of the APD with tight granularity, as shown in Fig. 15. The downward trend after the peak PDE is because of a difference in the mean of the Gaussian ROIC noise when the laser is on compared with when it is off. This is because of undershoot present in the tail of the impulse response of the ROIC. As more photons are incident upon the array, the mean of the noise shifts slightly, causing the curve to bend down. Of course this is not an issue during operation, because the threshold will never be set in the ROIC's noise floor and the operating point will be on the left side of the curve.

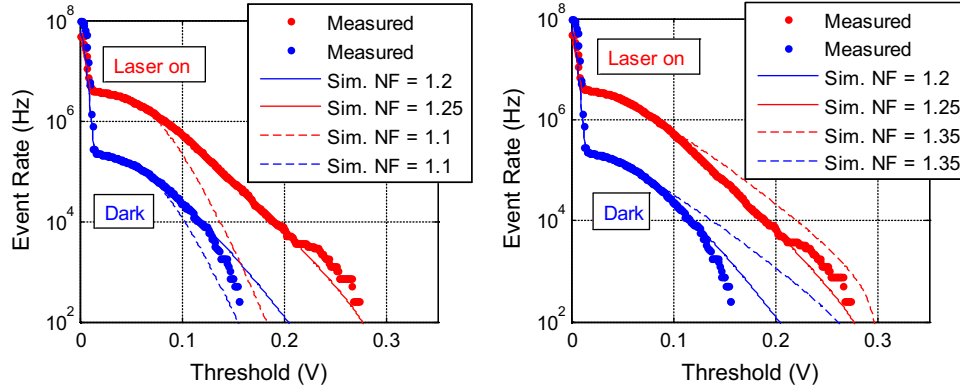


Fig. 15. Left: Best fit to a noise factor of 1.2-1.25 (solid line), with an excess noise factor of 1.1 also shown. Right: Same fit compared with an excess noise factor of 1.35.

CONCLUSIONS

The 2010 LMPC 2×8 arrays with photon counting sensitivity were successfully replicated with enhanced performance. It was experimentally verified that photons emitted by the ROIC artificially inflated the false event rate of the 2010 array, and the application of a single layer metal blocking layer and optimization of the ROIC biases reduced the false event rate by almost an order of magnitude to 100–200 kHz. Photon detection efficiencies of greater than 50% were routinely demonstrated for five arrays, with one array reaching 70%. High-resolution pixel-surface spot scans were performed and the junction diameters of the diodes were measured. The junction diameter was reduced from $31 \mu\text{m}$ to $22 \mu\text{m}$, resulting in a 4x increase in APD gain from 470 for the 2010 array to 1910 for A8327-8-2. Results from a 3D Monte Carlo random walk model were in good agreement with measured

junction diameters, rms jitter, and electron collection efficiency. Mean single photon SNRs of over 20 were demonstrated at excess noise factors of 1.2–1.3. A photon detection efficiency versus false event rate model was also generated; agreement with measured data was good.

REFERENCES

1. J.D. Beck, R. Scritchfield, P. Mitra, W. Sullivan III, A.D. Gleckler, R. Strittmatter, and R.J. Martin, *Proc. SPIE* 8033, 80330N (2011).
2. J.D. Beck, R. Scritchfield, P. Mitra, W.W. Sullivan III, A.D. Gleckler, R. Strittmatter, and R.J. Martin, *Opt. Eng.* 53, 081905 (2014).
3. M. Lanzoni, E. Sangiorgi, C. Fiegna, M. Manfredi, and B. Ricco, *IEEE Electron Device Lett.* 12, 341 (1991).
4. J. Rothman, L. Mollard, S. Gout, and J. Wlassow, *J. Electron. Mater.* 40, 1757 (2011).
5. J.D. Beck, M. Kinch, and X. Sun, *Opt. Eng.* 53, 081906 (2014).